

# The Influence of Photo-Induced Space Charge and Energetic Disorder on the Indoor and Outdoor Performance of Organic Solar Cells

Sebastian Beuel, Paula Hartnagel, and Thomas Kirchartz\*

Apart from traditional large-scale outdoor application, organic solar cells are also of interest for powering small, off-grid electronic devices indoors. For operation under the low light intensities that are typical for indoor application, a high shunt resistance is required calling for thick active layers in industrial processing to ensure maximum coverage. However, the thickness of an organic solar cell based on energetically disordered semiconductors is limited by space-charge effects from charged shallow defects under nonuniform generation. While other sources of space charge such as doping and asymmetric transport have been extensively discussed in previous studies, this work offers a theoretical analysis of this photo-induced space charge in shallow defects and visualizes how the space charge builds up with increasing light intensity with drift-diffusion simulations. It is shown that the effect particularly deteriorates the performance of an organic solar cell with high active-layer thickness and substantial energetic disorder. However, the simulations reveal that solar cells are less sensitive to these parameters under low light intensities due to a reduced density of photo-induced space charge. Therefore, a wider range of material systems and absorber thicknesses can be viable for indoor applications than one may initially expect from testing under 1 sun illumination.

those of classical inorganic solar cells,<sup>[1–3]</sup> organic photovoltaics has made substantial improvements in power-conversion efficiency in recent years.<sup>[4–8]</sup> This development was mostly fueled by the use of novel, small-molecule acceptor materials that replaced the previously used fullerene-based acceptors and led to improved absorption and reduced nonradiative recombination losses.<sup>[9–15]</sup> Despite the substantial amount of structural and conformational disorder present in these molecular semiconductor blends,<sup>[16–18]</sup> efficiencies of organic solar cells under standardized test conditions have been improved to >18%,<sup>[7,8]</sup> that is, substantially higher than that of highly disordered inorganic solar cells such as those based on amorphous Si absorber layers.<sup>[3]</sup> In addition, applications of organic photovoltaics beyond the traditional large-scale power generation market have become more important, both from a scientific and economic point of view.<sup>[19]</sup> In particular, organic solar cells are now frequently developed and optimized for indoor applications


## 1. Introduction

The development of solar cells based on semiconducting and solution processable molecules has a huge appeal due to the prospect of using low-cost and high-speed printing methods for device fabrication. While efficiencies are still trailing behind

such as powering small, off-grid electronic devices that constitute the internet of things,<sup>[20–24]</sup> A substantial part of device optimization for indoor applications is dealing with the increased influence of shunts at low light intensities and with the different spectrum of light emitting diodes (LEDs) or halogen lamps relative to the solar spectrum.<sup>[20,24]</sup> Industrial production of solar modules via roll-to-roll printing imposes additional constraints on device optimization both for indoor and outdoor applications. Reducing shunt formation during roll-to-roll printing over larger areas requires the use of substantially thicker active layers as is common in scientific laboratory environments.<sup>[25–29]</sup> A typical target thickness for industrial processing is around 300 nm and more<sup>[25,30]</sup> with most scientific publications focusing on active-layer thickness of  $\approx 100$  nm<sup>[7,8,31–33]</sup> while only few reports exist of highly efficient organic solar cells with absorber thicknesses > 300 nm.<sup>[28,34–38]</sup> A key challenge for achieving high efficiencies at thicknesses around 300 nm is the efficient collection of photo-generated charge carriers which can be hindered by recombination losses caused by fairly low mobilities and non-ideal electric field distributions caused by space-charge effects.<sup>[39–42]</sup> Recently, it has been shown that in particular the combination of charge stored in band tails caused by energetic disorder with the depth dependence of photogeneration leads to losses in short-circuit

S. Beuel, Prof. T. Kirchartz  
Faculty of Engineering and CENIDE  
University of Duisburg-Essen  
Carl-Benz-Str. 199, Duisburg 47057, Germany  
E-mail: t.kirchartz@fz-juelich.de

P. Hartnagel, Prof. T. Kirchartz  
IEK5-Photovoltaik  
Forschungszentrum Jülich  
Jülich 52425, Germany

 The ORCID identification number(s) for the author(s) of this article can be found under <https://doi.org/10.1002/adts.202000319>

© 2021 The Authors. Advanced Theory and Simulations published by Wiley-VCH GmbH. This is an open access article under the terms of the Creative Commons Attribution License, which permits use, distribution and reproduction in any medium, provided the original work is properly cited.

DOI: 10.1002/adts.202000319

current and subsequently efficiency that impose a strict limit on the maximum absorber layer thickness.<sup>[43]</sup> While the general principle has been shown and explained in Ref. [43], there are still several open questions: How does the amount of energetic disorder and the width of the band tail relate to device performance and how does the impact of space-charge effects change with reduced light intensity. The latter question is particularly important in the context of indoor photovoltaics, where substantially lower light intensities are available that might cause less photo-induced space-charge formation.

Here, we show the results of numerical drift-diffusion simulations of organic solar cells with energetic disorder to provide insights into the formation of photo-induced space charge. For this purpose, we first present the parameters and models required for the simulations. Then we study the impact of photo-induced space charge for different active-layer thicknesses and explain the observations on a microscopic scale. Afterwards, we examine the extent to which the severity of the band tails provokes different behavior with light intensity. In the scope of this work, we set a special focus on parameters that are of interest for future commercialization such as thick active layers and light intensities relevant for indoor application. Thereby, we provide theoretical understanding of the change in performance of an organic solar cell between 1 sun and low light condition and highlight how solar cells that show mediocre results under standard test conditions could still be viable candidates for indoor application.

## 2. Theoretical Background

The energetic disorder in organic semiconductors originates from their amorphous nature. Therefore, even above the highest occupied molecular orbital (HOMO) level and below the lowest unoccupied molecular orbital (LUMO) level, energetic defect states can be found. In analogy to amorphous silicon, these shallow defects are often called tail states.<sup>[43–48]</sup> Experimental data detecting tail states acquired from external quantum efficiency measurements or photothermal deflection spectroscopy can usually be well reproduced with an exponential density of band tail states.<sup>[15,49–54]</sup> Figure S1a, Supporting Information schematically illustrates the density of defect states defined by its characteristic slope  $E_U$ , the Urbach energy.<sup>[55]</sup> Typical values for the Urbach energy can be found between 30 and 80 meV<sup>[37,43,45,46,56]</sup> with state of the art material systems reaching Urbach energies close to thermal energy.<sup>[6,15,53,54]</sup> When a defect state near the HOMO level is occupied by a hole, its positive charge is localized at the position of the trap. The same principle holds for electrons that occupy the defect states near the LUMO level. The electrons add a negative charge to the total charge. Together with the free electron density  $n$  and free hole density  $p$ , the density  $p_t$  of trapped holes and density  $n_t$  of trapped electrons contribute to a total space-charge density  $\rho(x) = -n(x) - n_t(x) + p(x) + p_t(x)$  at a certain position  $x$  in the active layer.<sup>[48]</sup> Figure S1b, Supporting Information visualizes the charging of the defects states. The total charge density  $\rho(x)$  is further linked to the electric field  $F$  and the electrostatic potential  $\phi$  in the solar cell via Poisson's equation

$$\Delta\phi = -\nabla \cdot \vec{F} = -\frac{\rho}{\epsilon_0\epsilon_r} \quad (1)$$

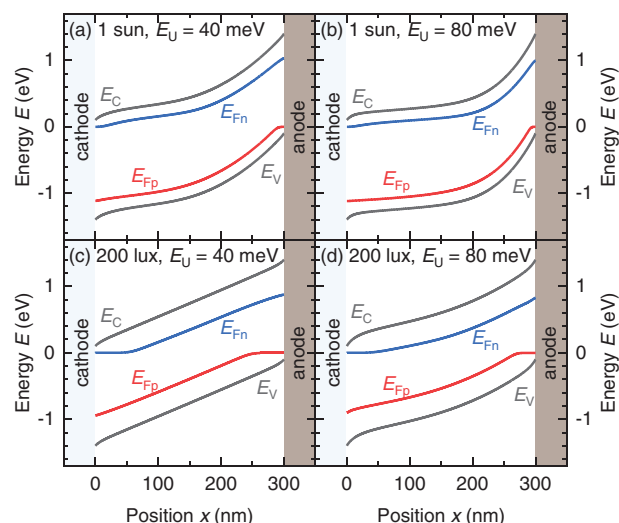


**Figure 1.** Energy diagram of organic solar cells with an active-layer thickness  $d = 300$  nm and recombination via tail states with an Urbach energy a,c)  $E_U = 40$  meV and b,d)  $E_U = 80$  meV. The illumination appears from the left at an intensity of a,b) 1 sun (AM1.5g spectrum) and c,d) 200 lux of a LED light source (see Figure S3, Supporting Information for the spectra). The generation current for the 200 lux illumination corresponds to  $1.6 \times 10^{-3}$  suns for reference. Whereas the energy bands remain mostly straight under low illumination, strong band bending occurs at the right contact under 1 sun. This photo-induced effect is more pronounced for a high Urbach energy.

with the dielectric constant  $\epsilon_0$  and the relative permittivity  $\epsilon_r$ . Therefore, a negative space charge causes a decrease in the electric field and a positive space charge causes an increase. That way, defect states do not only promote recombination in an organic solar cell but also alter the electric field and electrostatic potential by contributing to a local space charge.

Figure 1 displays such a space-charge induced change of the electrostatic potential in the form of band diagrams of a thick organic solar cell, which is illuminated from the cathode side. Similar to the observation by Wu et al.,<sup>[43]</sup> the band diagram in Figure 1a exhibits a shallow region at the illuminated contact and a steep increase of the conduction and valence band energy near the back contact. As the shallow defect states get more pronounced at an Urbach energy  $E_U = 80$  meV in comparison to 40 meV, more charge carriers can be trapped in proximity to the back contact causing an even further expansion of the shallow band region into the bulk. Since this phenomenon is evoked by illumination of the solar cell, it is interesting to note that for typical indoor light conditions of 200 lux under a light emitting diode (LED) in Figure 1c,d (corresponding to  $1.6 \times 10^{-3}$  suns under solar illumination), the bands remain mostly straight throughout the entire cell. This light-intensity dependent effect differs from the influence of other sources of space charge. Additional space charge due to doping, for instance, appears independent of the illumination condition.<sup>[43,57]</sup> Also, a light-intensity dependent space-charge region has been observed for asymmetric mobilities.<sup>[39,58–60]</sup> However, in the case of asymmetric mobilities the space charge builds up at the contact where the less mobile charge carriers are extracted.<sup>[39,58,59]</sup> In contrast, Wu et al. noted that the space-charge region in the absence of

asymmetric mobilities but presence of energetic disorder builds up at the contact opposite to the illuminated surface.<sup>[43]</sup> This unique behavior therefore requires further examination. Especially the light-intensity dependence of the space-charge effects implied by Figure 1 illustrates the need for a detailed analysis of the origin and the impact of space charge in tail states on the performance of organic solar cells.

To study the influence of energetic disorder on organic solar cells and to isolate the effect of space charge, numerical drift-diffusion simulations are a powerful tool. In this work, we use the Advanced Semiconductor Analysis (ASA) software, which was originally developed for amorphous silicon.<sup>[61]</sup> Alongside models for optical generation, ASA incorporates a solver of Poisson's equation, the continuity and transport equations with the finite differences method, which is typical for semiconductor simulation software.<sup>[47,62–64]</sup> In order to apply ASA to an organic solar cell, the effective medium approximation is used. It treats the bulk heterojunction as one semiconductor with the HOMO of the donor as the valence band and the LUMO of the acceptor as conduction band.<sup>[47,65]</sup> The usage of the effective medium approximation in ASA has yielded results that were in good agreement with experimental data in previous studies on organic solar cells.<sup>[44,66–69]</sup> The energetic disorder of the organic materials is implemented by including conduction and valence-band tails in the model. Thereby, charge-carrier recombination can take place between a free charge carrier in the energy bands and a trapped charge carrier in the band tails. In order to exclusively investigate the impact of the tail states, other recombination mechanisms such as band-to-band recombination and surface recombination are excluded in our model. These tail states are realized by a number of discretized energy levels that are treated as donor-like defects for the valence-band tails and acceptor-like defects for conduction-band tails. The charge in the energy levels is also accounted for in the process of solving Poisson's equation.

In simulations, there is the opportunity to suppress the influence of these space charges by choosing an infinitely high value for the relative permittivity. Thereby, one sets the variation of the electric field to zero and forces straight bands. Figure S2, Supporting Information illustrates how the case of no space-charge effects can help understanding their impact for a realistic permittivity with the example of a band diagram.

For the process of charge generation, we use a set of optical data to model a device consisting of an indium tin oxide electrode on quartz glass, a zinc oxide electron transport layer, poly[4,8-bis(5-(2-ethylhexyl)thiophen-2-yl)benzo[1,2-b;4,5-b']dithiophene-2,6-diyl-alt(4-(2-ethylhexyl)-3-fluorothieno[3,4-b]thiophene-2-carboxylate-2,6-diyl):5,5'-[[4,4,9,9-tetrakis(2-ethylhexyl)-4,9-dihydro-s-indaceno[1,2-b;5,6-b']dithiophene-2,7-diyl]bis(2,1,3-benzothiadiazole-7,4-diylmethylidene)]bis[3-ethyl-2-thioxo-4-thiazolidinone] (PTB7-Th:Eh-IDTBR) active layer, a molybdenum trioxide hole transport layer and a silver anode and to create a generation profile in ASA. The air mass 1.5global (AM1.5G) solar spectrum is used as the source of illumination when not stated otherwise. To further investigate the performance of organic solar cells under indoor conditions, we also apply the spectrum of a LED with a color temperature of 2700 K that fits the absorption of the active layer. Figure S3, Supporting Information displays the spectra of both light sources, whereas Figure S4, Supporting Information shows

**Table 1.** Parameters used for the simulation of organic solar cells in ASA when not stated otherwise.

Parameter	Symbol	Default value
Active-layer thickness	$d$	300 nm
Effective density of states conduction band/valence band	$N_{CB/VB}$	$10^{19} \text{ cm}^{-3}$
Effective bandgap energy	$E_{g,\text{eff}}$	1.5 eV
Injection barrier front/back contact	$\phi_{bf/bb}$	0.1 eV
Electron/hole mobility	$\mu_{e/h}$	$5 \times 10^{-4} \text{ cm}^2 \text{ V}^{-1} \text{ s}^{-1}$
Relative dielectric permittivity	$\epsilon_r$	3.8
Total density of conduction-/valence-band tail states	$N_{CBT}/N_{VBT}$	$10^{18} \text{ cm}^{-3}$
Urbach energy	$E_U$	40 meV
VBT hole/CBT electron capture coefficient	$\beta_1$	$10^{-8} \text{ cm}^3 \text{ s}^{-1}$
VBT electron/CBT hole capture coefficient	$\beta_2$	$10^{-12} \text{ cm}^3 \text{ s}^{-1}$

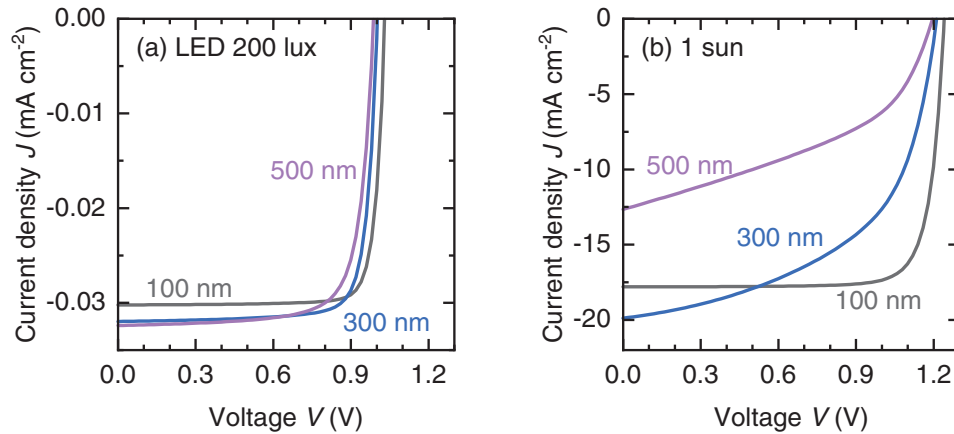
the resulting generation rate at 1 sun and 200 lux for different active-layer thicknesses. For instance, in a 300 nm thick device, the generation current for 200 lux illumination is equivalent to  $1.6 \times 10^{-3}$  suns. To provide further guidance for the units of light intensity used in this work, Figure S5, Supporting Information shows the illuminance in lux of the LED as a function of irradiance in suns for equivalent generation-current densities. In addition to the thickness and light intensity, we also vary the Urbach energy of the tail states. All the other parameters are kept constant throughout the simulations and are listed in Table 1.

Figure 2 shows some exemplary current-voltage characteristics of organic solar cells simulated with the parameters given in Table 1. The complete set of  $JV$ -characteristics under 1 sun illumination can be found in Figure S6, Supporting Information. Figure 2a illustrates the performance of solar cells with absorber thicknesses of 100, 300, and 500 nm under a low light intensity of 200 lux by a LED. Here, the open-circuit voltage  $V_{oc}$ , the fill factor  $FF$  and the short-circuit current density  $J_{sc}$  do not change drastically. The short-circuit current density  $J_{sc}$  increases with increasing thickness due to the gain in charge-carrier generation. However, in the case of 1 sun illumination in Figure 2b, the short-circuit current density  $J_{sc}$  increases from 100 to 300 nm but is significantly reduced for 500 nm. Along with the losses in fill factor, this behavior implies a reduced efficiency of charge-carrier collection outweighing the gain in photogeneration with increasing thickness. The different behavior in terms of active-layer thickness under high and low illumination therefore visualizes the presence of photo-induced effects in organic solar cells with inherent energetic disorder.

### 3. Results

#### 3.1. Space-Charge Effects Depending on Illumination and Absorber Thickness

Since organic solar cells with a thick active layer typically exhibit stronger space-charge effects, we focus our analysis on the light-intensity dependence of characteristic quantities of solar cells with absorber thicknesses of 100 to 500 nm. For the purpose of analyzing the efficiency of charge-carrier collection in these



**Figure 2.** Current density  $J$  as a function of applied voltage  $V$  for active-layer thicknesses of 100, 300, and 500 nm a) at low light intensity of 200 lux under a LED and b) at 1 sun illumination. The operating illumination condition greatly influences the overall shape of the  $JV$ -characteristics. Whereas the short-circuit current density  $J_{sc}$  increases with increasing active-layer thickness at 200 lux, it decreases for 500 nm at 1 sun, implying that there are charge collection problems for thick cells at 1 sun that do not exist at 200 lux.

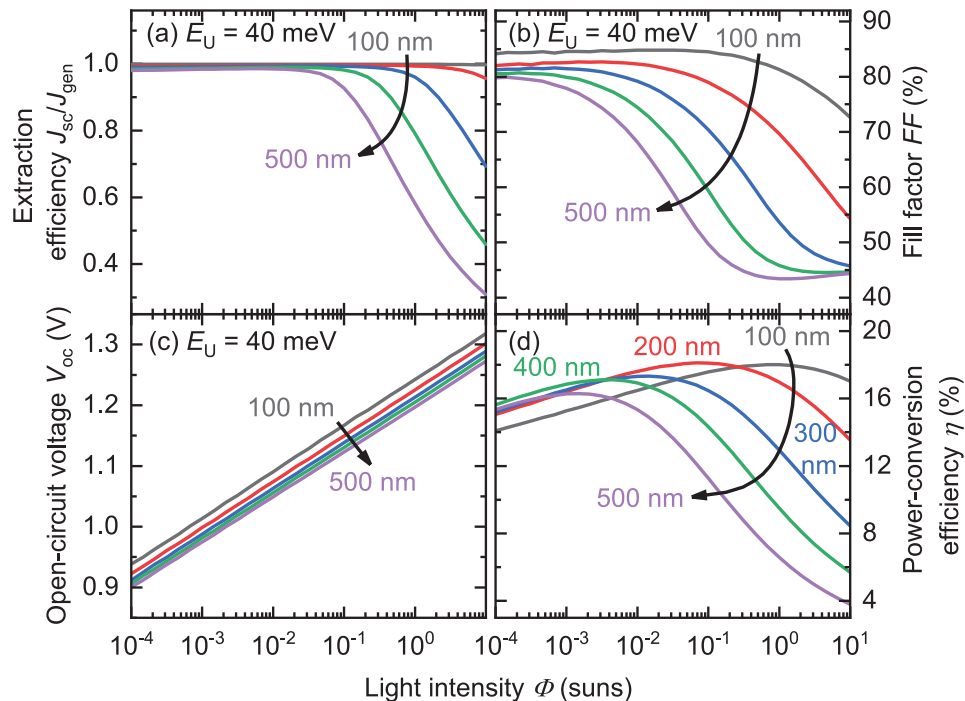


**Figure 3.** a) Short-circuit current density  $J_{sc}$  divided by the generation-current density  $J_{gen}$  corresponding to the light intensity  $\Phi$ , b) fill factor  $FF$ , c) open-circuit voltage  $V_{oc}$ , and d) power-conversion efficiency  $\eta$  as a function of light intensity  $\Phi$  for 100, 200, 300, 400, and 500 nm active-layer thickness  $d$ . The characteristic energy  $E_U$  of the exponential band tails is 40 meV. As  $d$  increases, the onset of the efficiency reduction shifts to lower light intensities mainly caused by a decrease in fill factor  $FF$ . The ratio  $J_{sc}/J_{gen}$  resembles an extraction efficiency, which is reduced for high light intensities.

devices, we define the extraction efficiency  $J_{sc}/J_{gen}$  as the ratio of the short-circuit current density  $J_{sc}$  and the generation-current density  $J_{gen}$ , which is shown in **Figure 3a** as a function of light intensity  $\Phi$ . The characteristic parameters fill factor  $FF$ , open-circuit voltage  $V_{oc}$  and power-conversion efficiency  $\eta$ , obtained from the  $JV$ -curves are shown in **Figure 3b–d**, respectively, as a function of light intensity  $\Phi$ . In **Figure 3a** the extraction efficiency  $J_{sc}/J_{gen}$  remains almost constant and close to unity at light intensities of  $10^{-4}$  to  $10^{-2}$  suns for all absorber thicknesses. As light

intensity is further increased, the extraction efficiency decreases, for which the onset of the reduction is located at lower light intensity for higher absorber thicknesses. A similar trend can also be observed in the curves of the fill factor  $FF$  in **Figure 3b**, where  $FF$  remains constant at first and decreases for higher light intensities. The onset of the reduction also exhibits a similar dependence on absorber thickness compared to the extraction efficiency, however, occurring at slightly lower light intensities. The difference between the onsets for strong light-intensity

dependence of fill factor and extraction efficiency can be explained considering the voltage range of these parameters. Whereas the ratio  $J_{sc}/J_{gen}$  resembles the charge-carrier extraction at the applied voltage  $V = 0$  V, the fill factor correlates to the charge-carrier extraction at  $V > 0$  V. Since the internal electric field  $F_{int} = (V_{built-in} - V)/d$  in the active layer is reduced by the applied voltage  $V$ , a change in the overall charge-carrier collection could be identifiable in the fill factor even at relatively low light intensities. In contrast, for the entire light-intensity range, the open-circuit voltage  $V_{oc}$  in Figure 3c increases exponentially with light intensity  $\Phi$  and is higher for smaller absorber-layer thicknesses. The slope of this linear increase on a logarithmic light-intensity scale reflects the ideality factor of the system which is supposed to remain constant as long as the Urbach energy is identical in all solar cells.<sup>[67]</sup> The increase of the open-circuit voltage with light intensity predominantly causes the initial rise of power-conversion efficiency in Figure 3d. However, the dependence on the active-layer thickness at low light intensities of  $10^{-4}$  to  $10^{-3}$  suns is reverse to the one of the open-circuit voltage  $V_{oc}$  and the fill factor  $FF$ . The reason for the enhanced power-conversion efficiency for thicker cells up to 400 nm is the charge-carrier collection decreasing not as quickly as the generation current increases with thickness. As a consequence, the short-circuit current density  $J_{sc}$  in Figure S7, Supporting Information is higher for thicker solar cells causing higher power-conversion efficiencies for increased absorber thickness. For light intensities above  $10^{-3}$  suns, the efficiency decreases with light intensity while the onset of the decrease successively shifts to lower light intensities with increasing thickness. These observations could be interpreted as a charge-carrier collection loss depending on the illumination condition, which gains in severity when the absorber thickness  $d$  is increased. Most notably, the decreasing trend of power-conversion efficiency is reflected in the  $FF$ -light intensity relation. This shift in maximum of the power-conversion with increasing absorber thickness is of special interest for the application of organic solar cells as a thick device, which is performing poorly under standardized test conditions but could still exceed the power-conversion efficiency of a 100 nm-device under low illumination. In addition, the spectrum of light sources providing such low illumination under indoor conditions can coincide with the absorption range of the organic semiconductors. Therefore, even higher power-conversion efficiencies can be observed when operating an organic solar cell under LED illumination as shown in Figure S8, Supporting Information.

Considering these efficiency gains for indoor applications, it could be helpful for solar cell design to estimate how a solar cell based on disordered materials performs under low light LED illumination relative to its performance under one-sun conditions. For this purpose, the ratio of power-conversion efficiency  $\eta_{LED}$  at the light intensity  $\Phi$  of a LED and the efficiency  $\eta_{1\text{ sun}}$  at 1 sun is shown in Figure 4. The 100 nm cell generally performs better under a LED than under solar illumination but shows no reduction of efficiency losses when operated under low light condition, since no significant power-conversion efficiency loss due to a photo-induced collection-efficiency reduction occurs. However, with increasing thickness, a gain in efficiency of up to 380% for a cell thickness of 500 nm can be identified. Considering that large scale processing for commercial application of organic solar cells

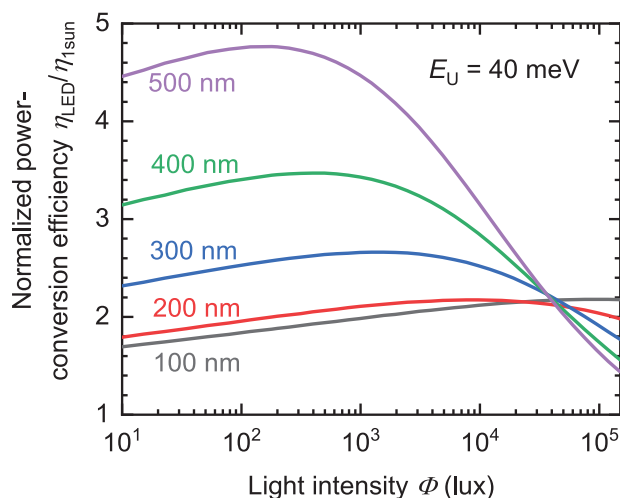


**Figure 4.** Ratio of power-conversion efficiency  $\eta_{LED}$  under LED illumination and the power-conversion efficiency  $\eta_{1\text{ sun}}$  at 1 sun from Figure 3 as a function of light intensity  $\Phi$  for 100, 200, 300, 400, and 500 nm active-layer thickness. The reduction of efficiency losses when operated under low light intensity increases for larger absorber-layer thicknesses.

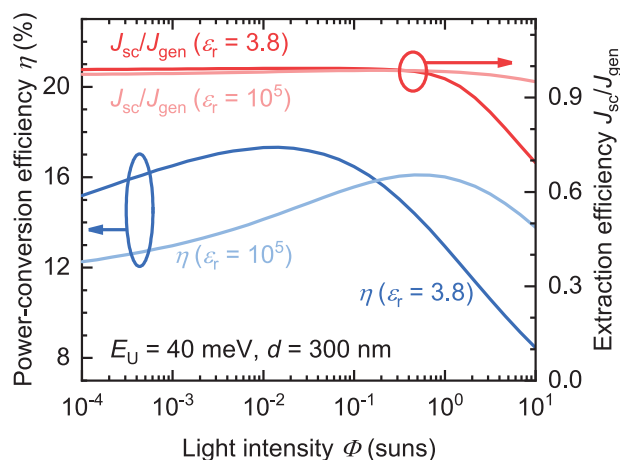


**Figure 5.** Light-intensity dependent power-conversion efficiency  $\eta$  and extraction efficiency  $J_{sc}/J_{gen}$  for an absorber-layer thickness of 300 nm and a relative permittivity of  $\epsilon_r = 3.8$  and  $\epsilon_r = 10^5$ . The characteristic energy  $E_U$  of the exponential band tails is 40 meV. The solar cell with  $\epsilon_r = 3.8$  performs better at low light intensities up to  $2 \times 10^{-1}$  suns than the device with  $\epsilon_r = 10^5$ . Under higher illumination, the device with suppressed space-charge effects is superior.

demands thicknesses above 300 nm, the reduction of photocurrent collection losses under indoor-light condition implies that high efficiencies in thick organic solar cells are easier to reach under low light conditions than under one sun conditions.

In order to analyze the impact of space charge on these efficiency gains, Figure 5 shows the power-conversion efficiency  $\eta$  alongside the extraction efficiency  $J_{sc}/J_{gen}$  as a function of light intensity  $\Phi$  for a solar cell with realistic permittivity and a solar cell with a relative permittivity that allows no field perturbation. For simplicity, we will in the following focus on an organic solar cell with an active-layer thickness  $d = 300$  nm and an Urbach energy  $E_U = 40$  meV. The understandings of the device physics obtained by this analysis, however, can be applied to other

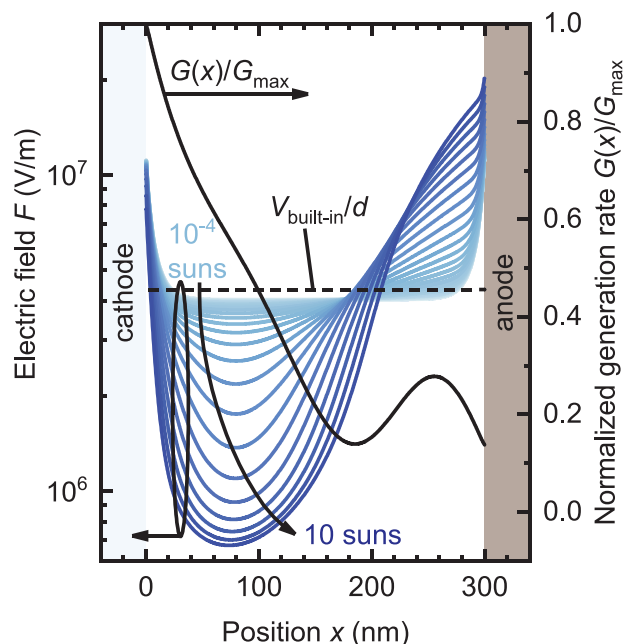


**Figure 6.** Electric field distribution along the position  $x$  in the active layer for different light intensities. A field reduction with increasing light intensity occurs at the side of illumination at the cathode ( $x = 0$  nm), where the normalized generation rate profile  $G(x)/G_{\max}$  has a global maximum. The deviation from the constant built-in field  $F_{\text{built-in}} = V_{\text{built-in}}/d$  indicated by the dashed line increases with illumination.

layer thicknesses and magnitude of tail states as well. In this case study, the impact of space charge can be observed in the extraction efficiency  $J_{\text{sc}}/J_{\text{gen}}$ . The decrease at high light intensities for a realistic permittivity is strong in comparison to the case of an arbitrarily high permittivity indicating that the collection of charges is hindered by an accumulation of space charge for a realistic permittivity. Similarly, the onset of the decrease in power-conversion efficiency  $\eta$  is shifted towards higher illumination in the absence of space-charge effects, once again indicating a space-charge limited performance. At low light intensities, however, the power-conversion efficiency  $\eta$  as well as the extraction efficiency  $J_{\text{sc}}/J_{\text{gen}}$  are lower for  $\epsilon_r = 10^5$  than for  $\epsilon_r = 3.8$  which might seem counterintuitive. To further understand this observation as well as the general impact of space charge, a deeper understanding of the microscopic effect of energetic disorder is required.

Therefore, we investigate the change of the electric field with light intensity in **Figure 6**. Close to the cathode, the electric field is high but suffers a steep decrease resulting in a low-field region. Towards the anode, the electric field increases again. With decreasing light intensity, the low-field region extends less towards the front contact and becomes less intense. Still, at very low light intensities, it remains below the value of the built-in field  $F_{\text{built-in}} = V_{\text{built-in}}/d$ , which corresponds to the electric field in a solar cell with infinitely high relative permittivity. Also, the electric field near the contacts exceeds the built-in field  $F_{\text{built-in}}$  and therefore enhances transport in these regions. Remarkably, under illumination of  $10^{-4}$  suns, this front region of enhanced transport extends around 20 nm into the bulk and thereby coincides with the region with the highest generation rate in the

solar cell. Herein lies a possible explanation for the superior performance at low light intensities of a solar cell with realistic permittivity compared to one with no space-charge effects that was observed in **Figure 5**. Since the electric field with space-charge effects is higher than the built-in field for high permittivity in the region, where most charge carriers are generated, more charge carriers can be extracted. Therefore, a space charge disturbing the electric field could also be beneficial for the solar cell performance which highlights the importance of understanding the formation of space charge.

To visualize these space charges, **Figure 7** shows the spatial density distribution of (a, b) free electrons  $n$  and holes  $p$  and (c, d) trapped electrons  $n_t$  and trapped holes  $p_t$  for different light intensities  $\Phi$  and for  $\epsilon_r = 10^5$  and  $\epsilon_r = 3.8$ , respectively. Here, the dashed lines highlight the region, where  $n \approx p$  or  $n_t \approx p_t$ . Both, free and trapped charge-carrier densities exhibit a similar shape, but the trapped charge-carrier densities are higher for lower light intensities. In the case of  $\epsilon_r = 10^5$ , the charge-carrier density of both, free electrons and free holes, increases in the bulk region of the absorber layer with  $\Phi$ , whereas the majority-charge carrier density at the contacts at  $x = 0$  nm and  $x = 300$  nm stays constant. In contrast, the minority-charge carrier density is higher at the illuminated contact than at the anode. When considering the difference of  $n + n_t$  and  $p + p_t$  around  $x = 0$  nm, it is clear that the net-space charge density  $\rho$  is determined by the free and trapped electron concentration as it is much higher than the hole concentrations in this region. Whereas the electrons are readily extracted, the holes that are still generated in large amounts propagate to the anode. At the position marked by the dashed line, the density of holes exceeds the electron density limiting the negative space-charge region to the first 80 nm. Towards the anode side of the solar cell, less and less charge carriers are generated due to the nonuniform generation profile. Hence, the holes that were generated at the illuminated contact pile up while there are few electrons to compensate this positive space charge. As a consequence of the high hole density, the trap states in the valence band tails are also more occupied, further amplifying the positive space charge. Whereas this space charge has no effect at  $\epsilon_r = 10^5$ , the accumulation of negative space charge at the cathode and of positive holes near the anode screens the electric field from the contacts for  $\epsilon_r = 3.8$ . The integrated charge from the front and back causing an electric field in the center of the cell is therefore lower, resulting in a low electric field as observed in **Figure 6**. This alteration of the electric field also affects the electron and hole densities themselves for  $\epsilon_r = 3.8$ . The interplay of electric field redistribution and reallocation of charge carriers determined by Poisson's equation results in the steady state charge-carrier densities displayed in **Figure 7b,d**. This spatial resolution of the free and trapped charge-carrier densities reveals a change in the space-charge effects with light intensity. Evidently, the space-charge regions at the front and back contact extend further into the bulk at low light intensities. The low electric field in the front region between 25 and 150 nm causes the charge carriers to pile up leading to no net-space charge in this region. As indicated by the dashed lines, the volume, where  $n \approx p$  and  $n_t \approx p_t$ , occupies more space of the absorber as light intensity increases. Thus, a photo-induced positive space charge that is increasingly localized at the back contact leads to more

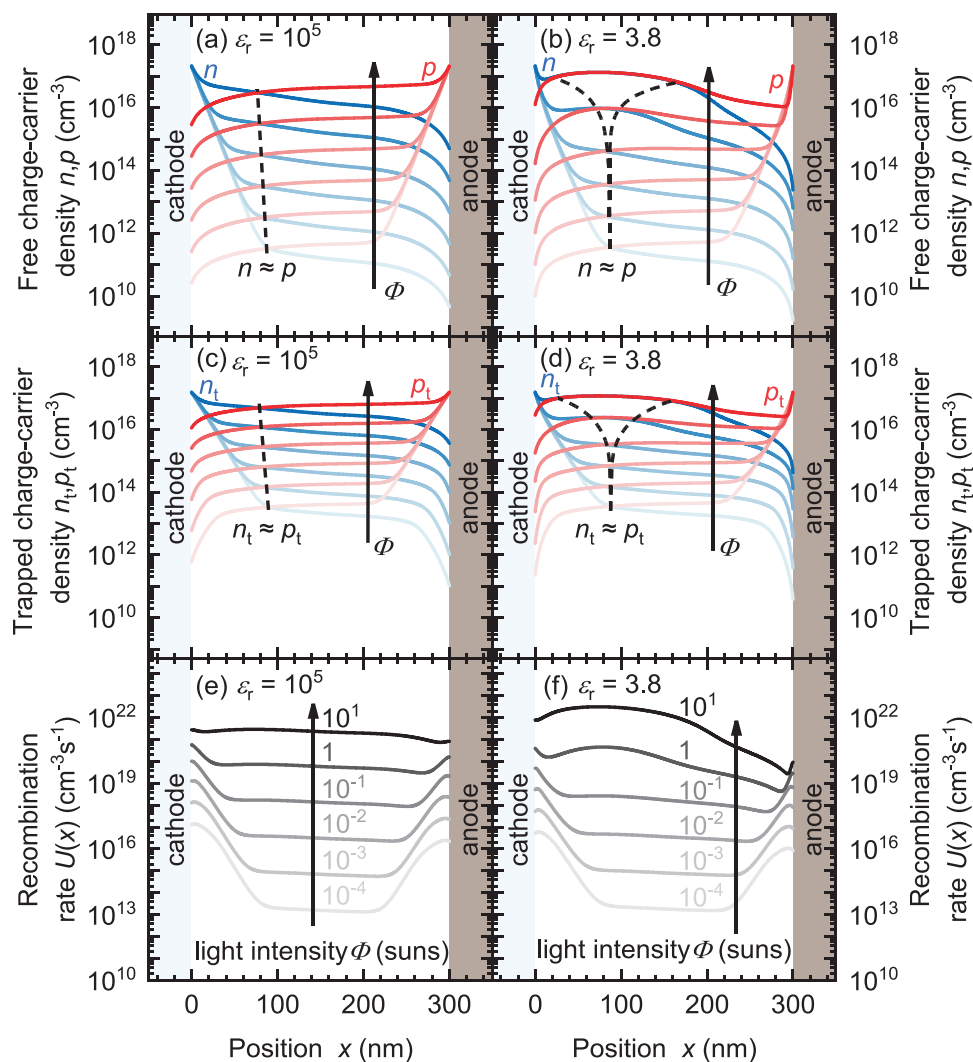


**Figure 7.** a,b) Spatial distribution of free electron density  $n$  and hole density  $p$ , c,d) spatial distribution of trapped electron density  $n_t$  and trapped hole density  $p_t$  and e,f) total recombination rate  $U(x)$  in the case of  $\epsilon_r = 10^5$  and  $\epsilon_r = 3.8$ , respectively, for light intensities  $\Phi$  ranging from around  $10^{-4}$  suns to 10 suns at  $V = 0$  V. The dashed lines in (a) and (b) highlight the region, where  $n \approx p$ , and in (c) and (d) the region, where  $n_t \approx p_t$ . The active-layer thickness is 300 nm and the characteristic energy  $E_U$  of the exponential band tails is 40 meV. Both, free and trapped charge-carrier densities exhibit a similar shape but the trapped charge-carrier densities are higher for lower light intensities. In the bulk region coinciding with the observed low-field region, an accumulation of both charge-carrier types occurs for  $\epsilon_r = 3.8$ , drastically increasing  $U(x)$  above  $10^{-1}$  suns.

and more screening of the electric field causing a region that limits charge transport.

The observed redistribution of charge-carrier densities upon illumination greatly influences the shape of the local recombination rate  $U(x)$  shown in Figure 7e for  $\epsilon_r = 10^5$  and Figure 7f for  $\epsilon_r = 3.8$ . In both cases, the recombination rate is highest in the proximity of the contacts for low light intensities. However, with higher light intensity, the bulk region, where both charge-carrier types scale with light intensity, gains in strength. This behavior of the recombination rate coincides with what has been observed for band-to-band recombination in previous studies.<sup>[70,71]</sup> As a result, the recombination rate in the case of  $\epsilon_r = 10^5$  is almost homogeneous at 10 suns. On the other hand, in the case of  $\epsilon_r = 3.8$ , the recombination rate starts to scale superlinearly with light intensity  $\Phi$  in the low-field region quickly surpassing the

recombination rate at the contacts. These variations in scaling of the recombination rate with illumination can possibly be reflected in the total recombination-current density  $J_{\text{rec}}$ . For further details on the relation of charge-carrier density, recombination rate and recombination-current density with illumination intensity, we refer to the Figures S9,S10, Supporting Information. Thereby, examining the spatially resolved recombination rate can further aid understanding the light-intensity dependent performance of an organic solar cell.

Herein, we have illustrated how space charge builds up under increasing light intensity screening the electric field from the contacts with the example of an organic solar cell with an active-layer thickness of 300 nm and an Urbach energy of 40 meV. In previous studies, it was already observed that the resulting low-field region in proximity of the illuminated contact

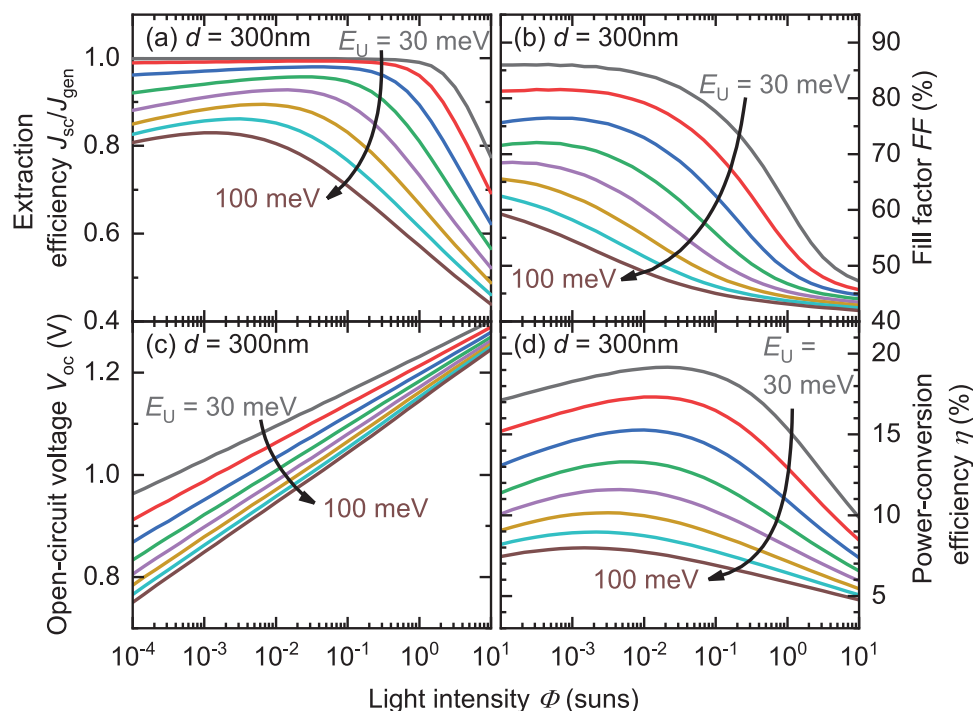


**Figure 8.** Light-intensity dependent a) extraction efficiency  $J_{sc}/J_{gen}$ , b) fill factor  $FF$ , c) open-circuit voltage  $V_{oc}$  and d) power-conversion efficiency  $\eta$  for different Urbach energies  $E_U$  ranging from 30 to 100 meV in steps of 10 meV and an absorber thickness  $d = 300$  nm. As the Urbach energy increases, the onset of efficiency reduction shifts to lower light intensities.

is more pronounced for Urbach tails with higher characteristic energy.<sup>[43,71]</sup> Hence, a thorough analysis of the photo-induced space-charge effect on the performance of organic solar cells with different Urbach energies under consideration of the illumination condition is required.

### 3.2. The Role of the Urbach Energy

As observed in Figure 1, the effects of photo-induced space charge that were discussed above are more prominent for tail states with a high Urbach energy  $E_U$ . As the defect states extend further into the energy gap, more space charge will accumulate altering the electric field. This effect is shown in the Figure S11, Supporting Information for a variety of Urbach energies. As a result, the  $JV$ -characteristic of an organic solar cell also changes with the shape of its Urbach tails. **Figure 8** shows the extraction efficiency  $J_{sc}/J_{gen}$  in (a), the fill factor  $FF$  in (b), the open-circuit voltage  $V_{oc}$  in (c) and the power-conversion efficiency  $\eta$  in (d) as a function of light intensity  $\Phi$  with an absorber thickness  $d = 300$  nm. The Urbach energy  $E_U$  is varied from 30 meV to 100 meV. As the density of states of the shallow defects extends further towards midgap for high Urbach energies  $E_U$ , all parameters decrease with increasing tail slope. For high Urbach energies, the extraction efficiency  $J_{sc}/J_{gen}$  increases slightly with light intensity, before decreasing for higher illumination. Whereas the extraction efficiency  $J_{sc}/J_{gen}$  exhibits a steep reduction for  $E_U = 30$  meV and light intensities above 1 sun, the decrease progressively flattens for higher Urbach energies as the recombination current diminishing the generation current scales with the tail

slope. The fill factor in Figure 8b shows a similar behavior while the onset of the decrease is shifted to lower light intensities. As a result, the fill factor decreases for all light intensities which is contrary to the experimental and theoretical results recently presented by Xiao et al.<sup>[72]</sup> They observed that solar cells with severe band tails exhibit a positive relation between the fill factor and light intensity.<sup>[72]</sup> As their discussion focusses on thin devices, Figure S12, Supporting Information shows the characteristic solar cell parameters for an active-layer thickness of 100 nm. Indeed, the results of our drift-diffusion simulations also feature an increase in fill factor with light intensities for high Urbach energies. However, this effect of the shallow defects competes with the influence of photo-induced space charge that is studied in this work. Figure 8 therefore shows that for thicker devices, space-charge effects due to energetic disorder outweigh the effect reported by Xiao et al. Besides the fill factor, the open-circuit voltage  $V_{oc}$  also exhibits a dependence on the Urbach energy. The slope of the open-circuit voltage  $V_{oc}$  determined by the ideality factor  $n_{id}$  increases with higher Urbach energies according to  $n_{id} = 2/(1 + kT/E_U)$ .<sup>[67,73,74]</sup> Evidently, the onset of the efficiency, fill factor and extraction efficiency reduction shifts to lower light intensities with higher Urbach energies  $E_U$  caused by a more pronounced photo-induced space charge sufficiently screening the internal electric field in the proximity of the cathode even at lower light intensities. By reducing the internal electric field, charge-carrier collection is hence degraded for high Urbach energies.

Generally, the performance of solar cell material systems degrades with higher Urbach energy as seen in Figure 8, but also the difference in performance between operating at high light intensity and low light intensity is dependent on the Urbach energy.

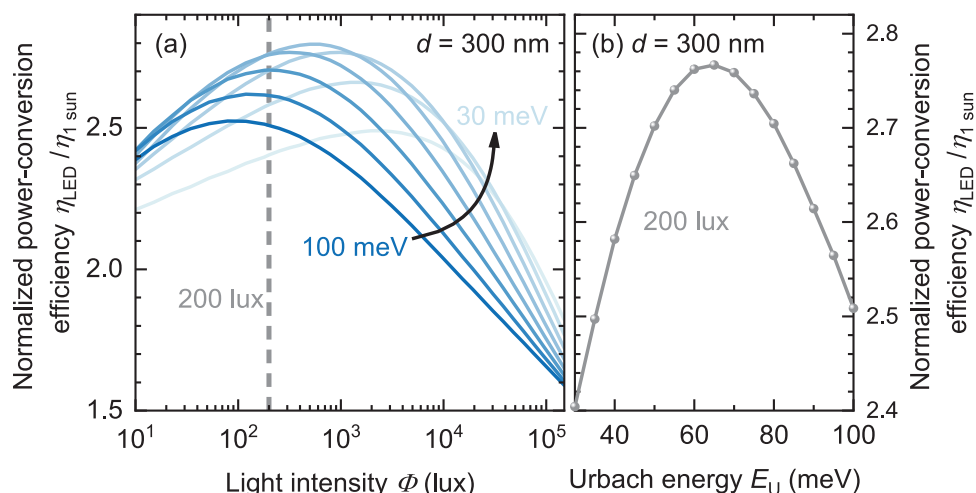


**Figure 9.** Power-conversion efficiency  $\eta_{LED}$  under a LED light source of an organic solar cell with absorber-layer thickness of 300 nm normalized to the power-conversion efficiency  $\eta_{1\text{ sun}}$  at 1 sun a) as a function of light intensity  $\Phi$  for Urbach energies  $E_U$  from 30 to 100 meV in steps of 10 meV and b) as a function of  $E_U$  at 200 lux (corresponding to  $1.6 \times 10^{-3}$  suns under solar illumination). The power-conversion efficiency gain according to (b), increases at first with  $E_U$  and then reaches a maximum gain of around 178%. This observation suggests, that even material systems with high Urbach energies, despite performing poorly at standard test conditions, could still be used at low light-intensity working condition.

Especially under a LED, high power-conversion efficiency gains can be expected as visualized in Figure S13, Supporting Information. Therefore, similar to the thickness dependence, a guideline can be provided for estimating the possible gain in performance of organic solar cell material systems with different Urbach energies  $E_U$  characterized at 1 sun illumination but operated under indoor condition, under which charge-collection losses can be minimized. This guideline could help to evaluate, whether a material system with high Urbach energy  $E_U$ , despite performing poorly under standard test conditions, could still be viable for indoor applications considering the reduction of efficiency losses.

Figure 9a shows the power-conversion efficiency  $\eta_{LED}$  of a solar cell with an active-layer thickness of 300 nm illuminated by a LED normalized to the power-conversion efficiency  $\eta_{1\text{ sun}}$  at 1 sun as a function of light intensity  $\Phi$ . The maximum power-conversion efficiency gain shifts to lower light intensities due to the onset of significant collection losses observed in Figure 8 also shifting to lower light intensities with increasing Urbach energy  $E_U$ . For a small Urbach energy of 30 meV, the power-conversion efficiency gain amounts to around 140% at 200 lux. More significantly, when a solar cell composed of a material system with a higher Urbach energy of 65 meV is measured under standard test conditions exhibiting poor performance, then the power-conversion efficiency could potentially increase by 178% at 200 lux working condition. The resulting power could be sufficient for certain applications. Organic solar cells with a high Urbach energy exhibit a photo-induced space charge at 1 sun and therefore perform better at low light intensities where there is no low-field region limiting the transport. In comparison, devices with a low Urbach energy encounter almost no impairment due to space-charge effects at any light intensity. However, the positive trend of the power-conversion efficiency gain with  $E_U$  at low light condition does not proceed for Urbach energies above 65 meV. As can be seen in Figure 9b, where the normalized efficiency  $\eta_{LED}/\eta_{1\text{ sun}}$  is shown as a function of Urbach energy  $E_U$  at 200 lux of the LED spectrum, the power-conversion efficiency gain decreases again to around

150% for  $E_U > 65$  meV. For Urbach energies  $E_U > 65$  meV, the electric-field redistribution could already be significant at light intensities around 200 lux. Therefore, material systems only perform significantly better under low light conditions when space-charge effects occur at 1 sun but not 200 lux.

Still, this analysis has shown that a material system that exhibits bad performance under standard test conditions due to severe band tails, but has favorable properties for low light application such as a high  $V_{oc}$ , or absorbance that matches the spectrum of the indoor-light source, should not be discarded before testing under low illumination condition. Our results imply, that a reduction of efficiency losses can be expected that might be sufficient for certain indoor applications.

## 4. Conclusion

In recent years, organic solar cells with low Urbach energies have exhibited record power conversion efficiencies highlighting the importance of energetic disorder on the performance of organic solar cells.<sup>[6,15,53,54]</sup> One of the key loss mechanisms in the presence of such tail states is the accumulation of space charge in the defect states, when charge-generation is nonuniform in the device. In this work, we use drift-diffusion simulations to visualize how this space charge builds up with increasing light intensity and how the electric field is altered in the process. The effect of space charge increases with thick active layers, with the degree of energetic disorder and with light intensity. However, our results imply that these devices that function poorly under high illumination can still undergo drastic efficiency increases under low light conditions. As the light induced space charge is less pronounced at for instance 200 lux, devices with thick active layers and high energetic disorder can still be viable candidates for indoor application.

In experimental work, these photo-induced space-charge effects together with resistive effects will determine the performance change of an organic solar cell under different

illumination conditions. Therefore, the understanding of the light-intensity dependent impact of energetic disorder presented in this work is crucial to correctly interpret experimental data and identify promising materials for indoor applications.

## Supporting Information

Supporting Information is available from the Wiley Online Library or from the author.

## Acknowledgements

T.K. and P.H. acknowledge funding by the Helmholtz Association. Open access funding enabled and organized by Projekt DEAL.

## Conflict of Interest

The authors declare no conflict of interest.

## Data Availability Statement

Research data are not shared.

## Keywords

absorber thickness, drift-diffusion simulations, shallow defects, tail states

- [1] C. Battaglia, A. Cuevas, S. De Wolf, *Energy Environ. Sci.* **2016**, 9, 1552.
- [2] P. K. Nayak, S. Mahesh, H. J. Snaith, D. Cahen, *Nat. Rev. Mater.* **2019**, 4, 269.
- [3] NREL, Best Research-Cell Efficiency Chart, <https://www.nrel.gov/pv/assets/pdfs/best-research-cell-efficiencies.20200218.pdf>, **2020** (accessed: November 2020).
- [4] H. Li, Z. Xiao, L. Ding, J. Wang, *Sci. Bull.* **2018**, 63, 340.
- [5] Y. Cui, H. Yao, J. Zhang, T. Zhang, Y. Wang, L. Hong, K. Xian, B. Xu, S. Zhang, J. Peng, Z. Wei, F. Gao, J. Hou, *Nat. Commun.* **2019**, 10, 2515.
- [6] Y. Cui, H. Yao, J. Zhang, K. Xian, T. Zhang, L. Hong, Y. Wang, Y. Xu, K. Ma, C. An, C. He, Z. Wei, F. Gao, J. Hou, *Adv. Mater.* **2020**, 32, 1908205.
- [7] Q. Liu, Y. Jiang, K. Jin, J. Qin, J. Xu, W. Li, J. Xiong, J. Liu, Z. Xiao, K. Sun, S. Yang, X. Zhang, L. Ding, *Sci. Bull.* **2020**, 65, 272.
- [8] Y. Lin, Y. Firdaus, F. H. Isikgor, M. I. Nugraha, E. Yengel, G. T. Harrison, R. Hallani, A. El-Labban, H. Faber, C. Ma, X. Zheng, A. Subbiah, C. T. Howells, O. M. Bakr, I. McCulloch, S. D. Wolf, L. Tsetseris, T. D. Anthopoulos, *ACS Energy Lett.* **2020**, 5, 2935.
- [9] D. Baran, T. Kirchartz, S. Wheeler, S. Dimitrov, M. Abdelsamie, J. Gorman, R. S. Ashraf, S. Holliday, A. Wadsworth, N. Gasparini, P. Kaienburg, H. Yan, A. Amassian, C. J. Brabec, J. R. Durrant, I. McCulloch, *Energy Environ. Sci.* **2016**, 9, 3783.
- [10] C. Yan, S. Barlow, Z. Wang, H. Yan, A. K. Y. Jen, S. R. Marder, X. Zhan, *Nat. Rev. Mater.* **2018**, 3, 18003.
- [11] P. Cheng, G. Li, X. Zhan, Y. Yang, *Nat. Photonics* **2018**, 12, 131.
- [12] M. Azzouzi, T. Kirchartz, J. Nelson, *Trends Chem.* **2019**, 1, 49.
- [13] M. Azzouzi, J. Yan, T. Kirchartz, K. Liu, J. Wang, H. Wu, J. Nelson, *Phys. Rev. X* **2018**, 8, 031055.

- [14] F. D. Eisner, M. Azzouzi, Z. Fei, X. Hou, T. D. Anthopoulos, T. J. S. Dennis, M. Heeney, J. Nelson, *J. Am. Chem. Soc.* **2019**, 141, 6362.
- [15] S. Liu, J. Yuan, W. Deng, M. Luo, Y. Xie, Q. Liang, Y. Zou, Z. He, H. Wu, Y. Cao, *Nat. Photonics* **2020**, 14, 300.
- [16] J. M. Frost, J. Kirkpatrick, T. Kirchartz, J. Nelson, *Faraday Discuss.* **2014**, 174, 255.
- [17] R. Noriega, J. Rivnay, K. Vandewal, F. P. Koch, N. Stingelin, P. Smith, M. F. Toney, A. Salleo, *Nat. Mater.* **2013**, 12, 1038.
- [18] X. Shi, V. Nádaždy, A. Perevedentsev, J. M. Frost, X. Wang, E. von Hauff, R. C. I. MacKenzie, J. Nelson, *Phys. Rev. X* **2019**, 9, 021038.
- [19] I. Mathews, S. N. Kantareddy, T. Buonassisi, I. M. Peters, *Joule* **2019**, 3, 1415.
- [20] Y. Cui, L. Hong, J. Hou, *ACS Appl. Mater. Interfaces* **2020**, 12, 38815.
- [21] Y. Cui, Y. Wang, J. Bergqvist, H. Yao, Y. Xu, B. Gao, C. Yang, S. Zhang, O. Inganäs, F. Gao, J. Hou, *Nat. Energy* **2019**, 4, 768.
- [22] C. L. Cutting, M. Bag, D. Venkataraman, *J. Mater. Chem. C* **2016**, 4, 10367.
- [23] M. E. Farahat, A. Laventure, M. A. Anderson, M. Mainville, F. Tintori, M. Leclerc, E. L. Ratcliff, G. C. Welch, *ACS Appl. Mater. Interfaces* **2020**, 12, 43684.
- [24] H. S. Ryu, S. Y. Park, T. H. Lee, J. Y. Kim, H. Y. Woo, *Nanoscale* **2020**, 12, 5792.
- [25] C. M. Amb, M. R. Craig, U. Koldemir, J. Subbiah, K. R. Choudhury, S. A. Gevorgyan, M. Jørgensen, F. C. Krebs, F. So, J. R. Reynolds, *ACS Appl. Mater. Interfaces* **2012**, 4, 1847.
- [26] A. Armin, M. Hamsch, P. Wolfers, H. Jin, J. Li, Z. Shi, P. L. Burn, P. Meredith, *Adv. Energy Mater.* **2015**, 5, 1401221.
- [27] T. Wang, X.-Y. Yang, P.-Q. Bi, M.-S. Niu, L. Feng, J.-Q. Liu, X.-T. Hao, *Sol. RRL* **2019**, 3, 1900087.
- [28] G. Zhang, K. Zhang, Q. Yin, X.-F. Jiang, Z. Wang, J. Xin, W. Ma, H. Yan, F. Huang, Y. Cao, *J. Am. Chem. Soc.* **2017**, 139, 2387.
- [29] J. Zhang, Y. Zhao, J. Fang, L. Yuan, B. Xia, G. Wang, Z. Wang, Y. Zhang, W. Ma, W. Yan, W. Su, Z. Wei, *Small* **2017**, 13, 1700388.
- [30] C. Duan, F. Huang, Y. Cao, *Polym. Chem.* **2015**, 6, 8081.
- [31] Q. Ma, Z. Jia, L. Meng, J. Zhang, H. Zhang, W. Huang, J. Yuan, F. Gao, Y. Wan, Z. Zhang, Y. Li, *Nano Energy* **2020**, 78, 105272.
- [32] D. Li, L. Zhu, X. Liu, W. Xiao, J. Yang, R. Ma, L. Ding, F. Liu, C. Duan, M. Fahlman, Q. Bao, *Adv. Mater.* **2020**, 32, 2002344.
- [33] X. Du, Y. Yuan, L. Zhou, H. Lin, C. Zheng, J. Luo, Z. Chen, S. Tao, L. S. Liao, *Adv. Funct. Mater.* **2020**, 30, 1909837.
- [34] J. Gao, W. Gao, X. Ma, Z. Hu, C. Xu, X. Wang, Q. An, C. Yang, X. Zhang, F. Zhang, *Energy Environ. Sci.* **2020**, 13, 958.
- [35] W. Gao, Q. An, M. Hao, R. Sun, J. Yuan, F. Zhang, W. Ma, J. Min, C. Yang, *Adv. Funct. Mater.* **2020**, 30, 1908336.
- [36] Y. Zhang, H. Feng, L. Meng, Y. Wang, M. Chang, S. Li, Z. Guo, C. Li, N. Zheng, Z. Xie, X. Wan, Y. Chen, *Adv. Energy Mater.* **2019**, 9, 1902688.
- [37] L. Ma, S. Zhang, H. Yao, Y. Xu, J. Wang, Y. Zu, J. Hou, *ACS Appl. Mater. Interfaces* **2020**, 12, 18777.
- [38] J. Qin, L. Zhang, Z. Xiao, S. Chen, K. Sun, Z. Zang, C. Yi, Y. Yuan, Z. Jin, F. Hao, Y. Cheng, Q. Bao, L. Ding, *Sci. Bull.* **2020**, 65, 1979.
- [39] T. Kirchartz, T. Agostinelli, M. Campoy-Quiles, W. Gong, J. Nelson, *J. Phys. Chem. Lett.* **2012**, 3, 3470.
- [40] P. Kaienburg, U. Rau, T. Kirchartz, *Phys. Rev. Appl.* **2016**, 6, 024001.
- [41] M. Stollerfoht, A. Armin, B. Philippa, D. Neher, *J. Phys. Chem. Lett.* **2016**, 7, 4716.
- [42] G. Zhang, R. Xia, Z. Chen, J. Xiao, X. Zhao, S. Liu, H.-L. Yip, Y. Cao, *Adv. Energy Mater.* **2018**, 8, 1801609.
- [43] J. Wu, J. Luke, H. K. H. Lee, P. Shakya Tuladhar, H. Cha, S. Y. Jang, W. C. Tsoi, M. Heeney, H. Kang, K. Lee, T. Kirchartz, J. S. Kim, J. R. Durrant, *Nat. Commun.* **2019**, 10, 5159.
- [44] T. Kirchartz, B. E. Pieters, J. Kirkpatrick, U. Rau, J. Nelson, *Phys. Rev. B* **2011**, 83, 115209.
- [45] J. Wu, J. Lee, Y.-C. Chin, H. Yao, H. Cha, J. Luke, J. Hou, J.-S. Kim, J. R. Durrant, *Energy Environ. Sci.* **2020**, 13, 2422.

- [46] S. A. Hawks, G. Li, Y. Yang, R. A. Street, *J. Appl. Phys.* **2014**, *116*, 074503.
- [47] T. Kirchartz, J. Nelson, *Top. Curr. Chem.* **2014**, *352*, 279.
- [48] R. C. I. MacKenzie, T. Kirchartz, G. F. A. Dibb, J. Nelson, *J. Phys. Chem. C* **2011**, *115*, 9806.
- [49] V. C. Nikolis, A. Mischok, B. Siegmund, J. Kublitski, X. Jia, J. Benduhn, U. Hormann, D. Neher, M. C. Gather, D. Spoltore, K. Vandewal, *Nat. Commun.* **2019**, *10*, 3706.
- [50] R. A. Street, A. Krakaris, S. R. Cowan, *Adv. Funct. Mater.* **2012**, *22*, 4608.
- [51] D. Venkateshvaran, M. Nikolka, A. Sadhanala, V. Lemaure, M. Zelazny, M. Kepa, M. Hurhangee, A. J. Kronemeijer, V. Pecunia, I. Nasrallah, I. Romanov, K. Broch, I. McCulloch, D. Emin, Y. Olivier, J. Cornil, D. Beljonne, H. Sirringhaus, *Nature* **2014**, *515*, 384.
- [52] A. J. Kronemeijer, V. Pecunia, D. Venkateshvaran, M. Nikolka, A. Sadhanala, J. Moriarty, M. Szumilo, H. Sirringhaus, *Adv. Mater.* **2014**, *26*, 728.
- [53] J. Yuan, C. Zhang, H. Chen, C. Zhu, S. H. Cheung, B. Qiu, F. Cai, Q. Wei, W. Liu, H. Yin, R. Zhang, J. Zhang, Y. Liu, H. Zhang, W. Liu, H. Peng, J. Yang, L. Meng, F. Gao, S. So, Y. Li, Y. Zou, *Sci. China: Chem.* **2020**, *63*, 1159.
- [54] Z. Zhang, Y. Li, G. Cai, Y. Zhang, X. Lu, Y. Lin, *J. Am. Chem. Soc.* **2020**, *142*, 18741.
- [55] F. Urbach, *Phys. Rev.* **1953**, *92*, 1324.
- [56] A. L. Jones, C. H. Y. Ho, P. R. Riley, I. Angunawela, H. Ade, F. So, J. R. Reynolds, *J. Mater. Chem. C* **2020**, *8*, 15459.
- [57] O. J. Sandberg, S. Dahlström, M. Nyman, S. Wilken, D. Scheunemann, R. Österbacka, *Phys. Rev. Appl.* **2019**, *12*, 034008.
- [58] D. Scheunemann, S. Wilken, O. J. Sandberg, R. Österbacka, M. Schiek, *Phys. Rev. Appl.* **2019**, *11*, 054090.
- [59] S. Wilken, O. J. Sandberg, D. Scheunemann, R. Österbacka, *Sol. RRL* **2020**, *4*, 1900505.
- [60] J. D. Kotlarski, P. W. M. Blom, *Appl. Phys. Lett.* **2012**, *100*, 013306.
- [61] M. Zeman, J. Krc, *J. Mater. Res.* **2008**, *23*, 889.
- [62] M. Burgelman, P. Nollet, S. Degraeve, *Thin Solid Films* **2000**, *361*, 527.
- [63] B. M. Omer, *Phys. Status Solidi A* **2016**, *213*, 2518.
- [64] B. E. Pieters, K. Decock, M. Burgelman, R. Stangl, T. Kirchartz, in *Advanced Characterization Techniques for Thin Film Solar Cells*, Vol. 2 (Eds.: D. Abou-Ras, T. Kirchartz, U. Rau), Wiley-VCH, Weinheim **2016**.
- [65] L. J. A. Koster, E. C. P. Smits, V. D. Mihailetschi, P. W. M. Blom, *Phys. Rev. B* **2005**, *72*, 085205.
- [66] I. Zonno, B. Krogmeier, V. Katte, D. Lübke, A. Martinez-Otero, T. Kirchartz, *Appl. Phys. Lett.* **2016**, *109*, 183301.
- [67] T. Kirchartz, F. Deledalle, P. S. Tuladhar, J. R. Durrant, J. Nelson, *J. Phys. Chem. Lett.* **2013**, *4*, 2371.
- [68] T. Kirchartz, P. Kaienburg, D. Baran, *J. Phys. Chem. C* **2018**, *122*, 5829.
- [69] F. Deledalle, T. Kirchartz, M. S. Vezie, M. Campoy-Quiles, P. Shakya Tuladhar, J. Nelson, J. R. Durrant, *Phys. Rev. X* **2015**, *5*, 011032.
- [70] U. Würfel, L. Perdigón-Toro, J. Kurpiers, C. M. Wolff, P. Caprioglio, J. Rech, J. Zhu, X. Zhan, W. You, S. Shoaee, D. Neher, M. Stollerfoht, *J. Phys. Chem. Lett.* **2019**, *10*, 3473.
- [71] P. Hartnagel, T. Kirchartz, *Adv. Theory Simul.* **2020**, *3*, 2000116.
- [72] B. Xiao, P. Calado, R. C. I. MacKenzie, T. Kirchartz, J. Yan, J. Nelson, *Phys. Rev. Appl.* **2020**, *14*, 024034.
- [73] C. van Berkel, M. J. Powell, A. R. Franklin, I. D. French, *J. Appl. Phys.* **1993**, *73*, 5264.
- [74] J. C. Blakesley, D. Neher, *Phys. Rev. B* **2011**, *84*, 075210.